



LAWRENCE
LIVERMORE
NATIONAL
LABORATORY

Recent Advances in Electron Tomography: TEM and HAADF-STEM Tomography for Materials Science and IC Applications

C. Kubel, A. Voigt, R. Schoenmakers, M. Otten, D. Su,
T.-C. Lee, A. Carlsson, H.-J. Engelmann, J. Bradley

November 11, 2005

Microscopy and Microanalysis

Disclaimer

This document was prepared as an account of work sponsored by an agency of the United States Government. Neither the United States Government nor the University of California nor any of their employees, makes any warranty, express or implied, or assumes any legal liability or responsibility for the accuracy, completeness, or usefulness of any information, apparatus, product, or process disclosed, or represents that its use would not infringe privately owned rights. Reference herein to any specific commercial product, process, or service by trade name, trademark, manufacturer, or otherwise, does not necessarily constitute or imply its endorsement, recommendation, or favoring by the United States Government or the University of California. The views and opinions of authors expressed herein do not necessarily state or reflect those of the United States Government or the University of California, and shall not be used for advertising or product endorsement purposes.

Recent Advances in Electron Tomography:

TEM and HAADF-STEM Tomography for

Materials Science and IC Applications

- TEM and STEM Tomography for Materials Science -

Christian Kübel^{1*}, Andreas Voigt¹, Remco Schoenmakers¹, Max Otten¹, David Su²,
Tan-Chen Lee², Anna Carlsson³, Hans-Jürgen Engelmann⁴, John Bradley⁵

¹ FEI Company, Applications Laboratory, Achtseweg Noord 5, 5651GG Eindhoven, The Netherlands.

² Taiwan Semiconductor Manufacturing Company, Ltd., Failure Analysis Division 9, Creation Road 1, Science-Based Industrial Park Hsin-Chu, Taiwan, R.O.C.

³ Haldor Topsøe A/S, Environmental & Materials Department, Research & Development, Nymøllevej 55, DK-2800 Lyngby, Denmark.

⁴ AMD Saxony LLC & Co KG, M/S E23-MA, Postfach 11 01 10, 01330 Dresden, Germany.

⁵ Institute for Geophysics and Planetary Physics, Lawrence Livermore National Laboratory, MS L-413, Livermore, CA 94550, USA.

* Corresponding Author: E-mail: ckuebel@nl.feico.com, Phone: +31 (40) 27-66101,
Fax: +31 (40) 27-66102

Abstract

Electron tomography is a well-established technique for three-dimensional structure determination of (almost) amorphous specimens in life science applications. With the recent advances in nanotechnology and the semiconductor industry, there is also an increasing need for high-resolution 3D structural information in physical sciences. In this paper, we evaluate the capabilities and limitations of TEM and HAADF-STEM tomography for the 3D structural characterization of partially crystalline to highly crystalline materials. Our analysis of catalysts, a hydrogen storage material, and different semiconductor devices shows that features with a diameter as small as 1-2 nm can be resolved in 3D by electron tomography. For partially crystalline materials with small single crystalline domains, TEM tomography provides reliable 3D structural information. HAADF-STEM tomography is more versatile and can also be used for high-resolution 3D imaging of highly crystalline materials such as semiconductor devices.

Keywords

3D Imaging, Electron Tomography, Transmission Electron Microscopy (TEM), High-Angle-Annular-Dark-Field Scanning Transmission Electron Microscopy (HAADF-STEM), Semiconductor Devices, Catalyst

Introduction

Both the characteristic dimensions of semiconductor devices and the feature size in nanostructured materials are decreasing with recent advances in nanotechnology and semiconductor manufacturing. This trend results in improved CPU performance and

higher storage capacities, but also in new materials such as catalyst with improved efficiencies (Breysse et al. 2003, Dhar et al. 2003). However, the smaller dimensions in these new materials also present new challenges for materials characterization and defect analysis including 3D metrology, surface roughness measurements, characterization of buried defects and simple understanding of complex 3D geometries. In principle, high-resolution transmission electron microscopy (HRTEM) and scanning transmission electron microscopy (STEM) techniques are routinely used to image materials with atomic resolution (Browning and Pennycook 2000, Spence 2002, Voyles et al. 2002, Kisielowski et al. 2001, Jia et al. 2003, James and Browning 1999). In addition, the combination with energy dispersive x-ray (EDX) and electron energy loss spectroscopy (EELS) techniques provides chemical information on a (sub)nanometer length scale (Batson 1999, Muller et al. 1999). However, as the feature sizes approach or become smaller than the finite thickness of typical TEM specimens, the limitations of two-dimensional methods for the analysis of inherently three-dimensional samples become apparent. When different features are projected on top of each other, the results of traditional imaging and analytical techniques cannot be interpreted easily. This makes accurate measurements for metrology difficult (Zschech et al. 2003, Lee et al. 2002) and even means that some defects or small particles might not be visible in a traditional 2D projections. In order to overcome these problems, 3D imaging (and analytical) techniques are needed to characterize complex nanostructures.

In this paper, we evaluate the use of different imaging techniques for electron tomography in order to produce general methods to characterize the three-dimensional structure of materials. We focus on the 3D characterization of a variety of different

materials by TEM and HAADF-STEM tomography. While, electron tomography has mainly been used for (almost) amorphous or weakly scattering crystalline materials, here we discuss the benefits and limitations of both methods for materials ranging from partially to highly crystalline.

Electron Tomography

Electron tomography is a technique providing nanometer scale resolution in 3D. Researchers in life science have been using bright-field (BF) TEM tomography for more than a decade to obtain 3D information on biological structures ranging from complete cells to protein complexes (Frank 1992, Baumeister et al. 1999, McIntosh 2001, McEwen and Marko 2001, Koster and Klumperman 2003, Sali et al. 2003). The 3D structural information is reconstructed digitally from a tilt-series of 2D projections, where 50-150 images are acquired by tilting the sample to cover a total tilt-range of about $\pm 70^\circ$ while simultaneously correcting for image shift and focus changes. The tilt-series is then processed off-line using back-projection techniques to reconstruct the “original” three-dimensional structure (Frank 1992).

In addition to life sciences, electron tomography has recently been used to characterize the 3D structure of a variety of different materials (Koster et al. 2000, Weyland et al. 2001, Buseck et al. 2001, Midgley and Weyland 2003). However, for materials science applications, care has to be taken that all micrographs in the tilt-series fulfill the projection criterion. This criterion states that in order to be suitable for tomography, the micrographs have to be true projections of the structure to be reconstructed. At the very least, this implies that the recorded signal must vary strictly monotonically with

(mass)thickness. This projection requirement is met for BF-TEM micrographs of amorphous materials, where mass-thickness is the dominant contrast mechanism (with small non-monotonic contributions due to defocus effects, e.g. Fresnel fringes). However, the projection criterion is not satisfied for BF-TEM images of strongly scattering crystalline materials where diffraction contrast typically dominates the image formation. Therefore, BF-TEM tomography is only of limited value for materials science applications.

Other imaging techniques are needed as a general solution for the 3-dimensional characterization of (crystalline) materials by electron tomography. These imaging techniques must strongly reduce diffraction effects and fulfill the projection criterion even in the presence of highly crystalline materials. In principle, energy filtered TEM (EFTEM) and high-angle annular dark-field (HAADF) STEM imaging are two such alternative techniques. The contrast observed in background-subtracted energy-loss (EFTEM) images of thin samples is, to a first approximation, a function of the projected amount of an atomic species in a specimen. However, diffraction effects also affect the inelastically scattered electrons and induce some diffraction contribution in the elemental maps. More importantly, the elemental maps exhibit a monotonic thickness behavior only for thin samples, whereas the signal decreases drastically for thicker materials. This limits the application of EFTEM tomography to a thickness of less than about 0.7λ at the maximum tilt-angle (Weyland and Midgley 2003). For example, for a $\pm 65^\circ$ tilt-series of a carbonous sample at 200kV, this limits the thickness to about 35 nm. For materials with a higher density, the thickness is even more limited, which makes this

technique unsuitable for typical ultra-microtomed or focused ion beam (FIB) prepared samples.

However, HAADF-STEM imaging does not suffer from the same limitations and potentially provides a more general solution for electron tomography of crystalline materials. As a first approximation, HAADF-STEM imaging results in Z-contrast images due to Rutherford scattering, where the intensity is a function of the atomic number ($Z^{1.7-2}$) and is a linear function of the projected sample thickness. In all practical applications, the collection angle is limited, resulting in a small diffraction contribution to the HAADF signal, which is typically negligible for collection angles higher than 70 mrad at 200kV. The only visible artifacts in HAADF-STEM tilt-series are due to channeling effects when a crystal is imaged exactly along a major zone-axis. However, as the major zone axes are only encountered rarely during a tilt-series, the overall effect on the 3D reconstruction is small, even for highly crystalline materials.

In this paper, we present our evaluation of TEM and HAADF-STEM electron tomography for various types of applications. In determining which technique to use, the reliability of the 3D reconstruction (despite slight deviations from the projection criterion) was the most crucial aspect. In addition, we considered the kind of features that can be resolved for materials in 3D (resolution) together with practical considerations such as ease-of-use and time-to-results. These practical considerations will also help to determine which application fields will potentially benefit from electron tomography. For this overview, we have been looking at three different types of materials: catalysts, a hydrogen storage material, and semiconductor devices. These samples allow us to cover the range from nanocrystalline materials with high defect densities to highly

crystalline devices with “large” single-crystalline domains. We did not consider EFTEM tomography due to the strong sample thickness restrictions, but we will discuss the advantages of TEM and HAADF-STEM tomography for the different materials and illustrate what information can be obtained.

Methods

Tomographic Data Acquisition

Single axis tilt-series for TEM tomography were acquired automatically on a FEI Tecnai Sphera (T20 Twin) using the FEI XPlore3D Tomography Suite. The microscope was operated in TEM mode with parallel illumination under semi-low-dose conditions[†]; no objective aperture was used to minimize the influence of diffraction effects and the defocus was set to -1 to -2 micron depending on the magnification. The TEM projections were acquired on a bottom-mounted slow scan CCD camera with 1024 x 1024 pixels (Gatan 794). Typically 131 electron micrographs were collected over an angular range of $\pm 65^\circ$ in 1° steps. Re-centering and re-focusing of the area of interest after tilting were

[†] The dose used to image the area of interest was minimized by blanking the beam between CCD exposures. The images themselves were taken at a dose of 500-10000 e/nm² depending on the sample and the magnification. Tracking was done only based on the tilt-series itself and therefore did not add any dose to the imaging process. Focusing was done on the area of interest every 5-10 images with a reduced exposure time, adding an additional dose of about 10-20% to the tilt-series.

True low-dose conditions can also be used in XPlore3D, but it was not necessary to use for the examples presented in this article.

done automatically by combining precalibration of the goniometer movements (Ziese et al. 2002) with active shift and focus measurements as implemented in the XPlore3D acquisition software. Typically, the active focus measurement was done every 5-10 tilt-increments using the beam-tilt induced image shift (Koster et al. 1987) and the active shift correction was done based on the acquired tilt-series itself. The total acquisition time for this TEM tomography tilt-series was approximately 30-45 minutes.

Single axis tilt-series for HAADF-STEM tomography were acquired automatically on a Tecnai F20 ST using the XPlore3D 2.0 Tomography Suite. The microscope was operated in HAADF-STEM mode with a nominal spot size of 0.2 nm. A small camera length of 70-100 mm was used for the HAADF-STEM signal collection to efficiently minimize diffraction effects. Scanned images with 1024x1024 or 2048x2048 pixels were acquired using a frame time of 15-30 sec. Typically 71 electron micrographs were collected over an angular range of $\pm 70^\circ$ in 2° steps. Again, re-centering and re-focusing were done automatically. Typically, the active focus measurement was done every 2-3 tilt-increments based on an automatic analysis of a small HAADF-STEM through-focus series. The focus was adjusted automatically during the acquisition of each frame to compensate for the tilt-induced height change of the sample (dynamic focus). The active shift correction was done based on the acquired tilt-series. The total acquisition time for such a HAADF-STEM tilt-series is about 45-90 minutes.

Image Processing and 3D Reconstruction

After acquisition, the tilt-series data is transferred to an off-line computer for image processing and reconstruction. We were using IMOD Version 2.7 (by David

Mastronarde, James Kremer, and Rick Gaudette at the Boulder Laboratory for 3-Dimensional Electron Microscopy of Cells) and our own Inspect3D Version 1.0 software for post processing. Both software packages were installed on a Dell Precision 530 with a dual 2.0 GHz Intel Xeon processor and 2 GB of RAM. IMOD is running under RedHat Linux Version 7.3 and Inspect3D is running under Windows 2000/XP.

Before tomographic reconstruction, the tilt-series has to be aligned precisely with respect to a common tilt-axis, thereby minimizing both blurring of small features and artifacts in the reconstruction. In IMOD this is achieved by a combination of rough cross-correlation alignment and least-square fitting of fiducial markers such as gold nano particles. Typically 15-30 markers (well distributed over the imaged area) were tracked throughout the tilt-series and were used as the basis to refine x-y image shifts, image rotation and magnification (adjustment typically less than 0.1-0.5%). In some cases, the tilt-angle was also refined within strict limits (less than 0.1° adjustment between successive images and less than 2° adjustment over the whole tilt-series). Following the image alignment, the 3D volume was reconstructed using weighted back-projection.

In case of Inspect3D, the tilt-series alignment was done only using cross-correlations, thereby eliminating the need for marker tracking (and the presence of markers on the sample). An iterative approach has been implemented in Inspect3D; by adding the shifts measured from all iterations prior to applying them to the original data set for the final sub-pixel alignment, it is ensured that pixel gray values are interpolated only once. In addition, a final step to improve the position and orientation of the tilt axis is done by a manual procedure where these tilt axis parameters can be interactively adjusted until reconstruction artifacts are minimized (Weyland 2001). After the image alignment, the

3D volume is reconstructed using real-space weighted back-projection (Gilbert 1972).

Visualization

Visualization of the reconstructed volume is done either by volume- or by surface rendering using Amira Version 3.0 (by TGS software). The volume rendering was optimized by adjusting the threshold for color-coding and the transparency of the different components. For the surface rendering, a first approximation of the different surfaces was obtained by thresholding of the data. However, due to the artifacts induced in the reconstruction by the weighting filters and the missing wedge, the contours were edited manually to enhance the visualization.

Materials

Oil-Refining Catalyst #1

The commercial catalyst from Haldor Topsøe A/S is based on a highly porous alumina support material with small MoO_3 particles as the active catalyst. The active catalyst was embedded in Struers Specifix-20 and sectioned on a RMC MT-XL to a thickness of 150 nm. Five and fifteen nm gold markers were applied to the sample on the TEM grid from an aqueous solution (Department of Cell Biology, University of Utrecht) and the stabilizing detergent was cleaned off with deionized water.

TEM tomography data sets were acquired on a Tecnai Sphera as described above. The microscope was operated at a nominal magnification of 25000x resulting in a pixel size of 0.69 nm at the specimen level; the defocus was set to -2 micron. The tilt-series was acquired automatically over a tilt-range of -63° to $+60^\circ$ in 1° steps.

IMOD was used to align the tilt-series by cross-correlation followed by marker tracking, where refinement of the average tilt-axis orientation and refinement of the magnification were enabled during alignment. The residual error of the marker tracking was 0.9 pixels. The 3D volume was reconstructed by weighted back-projection using IMOD.

Oil-Refining Catalyst #2

The second catalyst sample is a naphtha reforming catalyst containing 1 to 1.5 nm Pt particles on a fine-grained alumina support. The catalyst was crushed, dispersed in ethanol and deposited on a holey carbon support foil on a standard TEM grid. Five and fifteen nm gold markers were applied to the sample on the TEM grid from an aqueous solution (Department of Cell Biology, University of Utrecht) and the detergent was cleaned off with deionized water.

TEM tomography data sets were acquired on a Tecnai Sphera as described above. The microscope was operated at a nominal magnification of 68000x, resulting in a pixel size of 0.23 nm at the specimen level; the defocus was set to -1.5 micron. The tilt-series was acquired automatically over a tilt-range of $\pm 65^\circ$ in 1° steps.

The tilt-series alignment was performed with Inspect3D by iterative cross-correlation techniques using image filters to enhance the gold markers during cross-correlation. The overall tilt-axis orientation and shift were optimized semi-automatically by minimizing reconstruction artifacts of the gold markers at various positions in the 3D volume. The reconstructed volume was binned by a factor of 2 to improve the signal to noise (before binning, 1000 slices in z-direction were calculated based on only 131 input images).

High surface area hydrogen storage medium (HSM)

The HSM was ultra-microtomed to a nominal thickness of 200 nm. This material is an advanced Mg-Ni based hydrogen storage alloy for use in NiMH batteries. The sample was provided courtesy of Ovonic Battery Company (Fetconko et al. 1997, 2003). Five and fifteen nm gold markers were applied to the sample on the TEM grid from aqueous solution (Department of Cell Biology, University of Utrecht) and the detergent was cleaned off with deionized water.

TEM tomography data sets were acquired on a Tecnai Sphera as described above. The microscope was operated at a nominal magnification of 29000x, resulting in a pixel size of 0.59 nm at the specimen level; the defocus was set to -2 micron. The tilt-series was acquired automatically over a tilt-range of $\pm 65^\circ$ in 1° steps.

HAADF-STEM tomography data sets were acquired on a Tecnai F20 ST using an alpha version of the XPlore3D Tomography Suite (dynamic focus not implemented at the time). Micrographs with 1024 x 1024 pixels were acquired at a nominal magnification of 320 kx resulting in a pixel size of 0.27 nm at the specimen level. The tilt-series was acquired automatically over a range of $\pm 72^\circ$ in 2° steps.

IMOD was used to align the tilt-series by cross-correlation followed by marker tracking, where refinement of the average tilt-axis orientation and refinement of the magnification were enabled during alignment. The residual error of the marker tracking was 0.8 pixels (TEM data set) and 0.9 pixels (STEM data set). The 3D volume was reconstructed by weighted back-projection using IMOD and filtered with a 3D median filter with a kernel size 3 in Amira for noise reduction.

Copper Interconnect Lines

The cross-section of copper interconnect lines in an AMD CPU was prepared by FIB on a FEI DB235. The TEM lamella was thinned and polished to a thickness of 150 nm, lifted out externally and deposited on a Quantifoil TEM grid (for details about the method see Young et al. 1998). Prior to the tomographic imaging, the sample had been used for extensive spectrum imaging, which generated some holes in the copper due to the high beam currents used for the elemental mapping.

HAADF-STEM tomography data sets were acquired on a Tecnai F20 ST using an alpha version of the XPIore3D Tomography Suite (dynamic focus not implemented at the time). Micrographs with 2048 x 2048 pixels were acquired at a nominal magnification of 40 kx, resulting in a pixel size of 1.5 nm at the specimen level. The tilt-series was acquired automatically over a range of -68° to $+70^{\circ}$ in 2° steps.

Inspect3D was used to align the tilt-series by an iterative cross-correlation approach and to reconstruct the 3D volume by weighted back-projection. The reconstructed volume was visualized by surface rendering using Amira. The surfaces obtained automatically by density thresholding were edited manually to enhance the barrier layer and reduce noise prior to 3D visualization.

Flash-Memory Cell

The cross-section of a flash-memory cell from TSMC was prepared by FIB on a FEI DB835. The TEM lamella was thinned to a thickness of 180 nm by the ion beam, lifted out externally and deposited on a carbon film with pre-adsorbed 10 nm gold particles.

HAADF-STEM tomography data sets were acquired on a Tecnai F20 ST using the XPIore3D Tomography Suite. Micrographs with 1024 x 1024 pixels were acquired automatically over a tilt-range of -66° to +67° in 1° steps.

IMOD was used to align the tilt-series by cross-correlation followed by marker tracking, where refinement of the average tilt-axis orientation and refinement of the magnification were enabled during alignment. The residual error of the marker tracking was 0.9 pixels. The 3D volume was reconstructed by weighted back-projection using IMOD and filtered using a 3D median filter with kernel size 3 in Amira for noise reduction. After binning the reconstructed volume by a factor of 2, the structure of the memory cell was visualized by surface rendering using Amira. The polysilicon surfaces obtained automatically by density thresholding were edited manually to enhance the silicon borders.

The aligned tilt-series was also reconstructed using the iterative back-projection algorithm SIRT algorithm (Gilbert 1972) as implemented in an alpha-version of Inspect3D 2.0. Twenty iterations were performed for the SIRT reconstruction.

Results and Discussions

Catalyst Materials

Classical catalysts consist of a nano crystalline porous support material covered by a high density of nano particles providing the active catalyst sites. In addition to the size and shape distribution of the active catalyst particles, the quality of a catalyst is crucially affected by the shape, pore size distribution and permeability of the support material as well as the distribution of the active catalyst on the support material. Simple 2D

projections mainly reveal information about the average density in the projected area, but the shape and pore size of the support material are difficult to interpret. Furthermore, especially for thick samples, it can be difficult to unambiguously identify the catalyst particles themselves. Figure 1 exemplifies this problem for an alumina based oil-refining catalyst from Topsoe. The TEM projection reveals a lower density in the center of the imaged area, but it is difficult to estimate further details of the shape and size distribution of the support material, especially in the high-density areas.

FIGURE 1

In contrast, the 3D volume reconstructed by TEM tomography (for details see Materials and Methods) reveals significantly more details (Figure 2 and 3). For example, the support material has a sheet-like structure (Figure 3) appearing as a line in the slices through the reconstructed volume. The average thickness of the sheets is 4-5 nm, but thicknesses of up to 8 nm were also observed. The sheets are observed in all orientations (within the limit of the missing wedge due to the tilt-series acquisition[‡]) forming pores of different diameter and shape. In the large central pore, the support sheets are significantly more extended than the sheets found in the densely packed areas.

[‡] Objects only exhibiting Fourier components in the missing wedge are not observed by weighted back-projection or only with reduced intensity. This means, that thin sheets oriented perpendicular to the electron beam are not visible in a tomogram obtained by weighted back-projection.

Based on the tomography results, it is expected that properties of the pore system, such as connectivity and tortuosity, can be determined. Since many reactions are diffusion limited, the transport properties have a great influence on the activity of the catalyst. In order to model and understand these transport properties, a realistic model of the pore system is needed.

FIGURE 2

FIGURE 3

The magnification used to record the data for the tomogram in Figure 2 is just high enough to recognize the actual catalyst particles. Based on Figure 2, it appears that the particles are distributed fairly uniformly. However, to reveal more details about the particle and size distribution, a higher magnification would be needed.

To illustrate the characterization of the actual catalyst particles, a higher magnification tilt-series has been recorded for a similar catalyst. This catalyst is also based on an alumina support, but in this case the active part of the catalyst were Pt nano particles. Figure 4 shows a central image from the tilt-series, which mainly reveals the support material as well as the gold markers used for image alignment. The active catalyst is also visible, but it is difficult to unambiguously identify the particles in a single projection of this 150 nm thick area.

FIGURE 4

The volume reconstructed from the high-magnification tilt-series shown in Figure 4 reveals the overall structure of the support material as well as the 3D distribution of the Pt nano particles (Figure 5). The contrast in the reconstructed volume is significantly better than in the original projected images, enabling a clear identification of the Pt catalyst particles. Whereas the Pt particles are projected on top of 150 nm of alumina support in the original projections, the contrast in the reconstructed volume depends only on the density of the Pt particles compared to the alumina support.

FIGURE 5

The resolution in the reconstructed volume is not only sufficient to detect the Pt particles, but furthermore enables a statistical analysis of the size distribution. The diameter of ~40 particles in an x-y slice and 25 particles in an x-z slice through the reconstructed volume was analyzed by means of line profiles. The FWHM[§] in the line profile was used to estimate the particle diameter (Figure 6). The average particle diameter measured in the x-y plane is 1.7 ± 0.4 nm, whereas the average diameter measured in z-direction is 2.1 ± 0.5 nm. The difference is due to the elongation of the reconstructed volume in z-direction due to the missing cone (Rademacher 1988).

[§] The tomographic reconstruction does not have an absolute intensity scale, which makes it difficult to define the zero-line to estimate the FWHM in the line profiles. Therefore, the average background intensity was used as reference to estimate the FWHM.

$$\varepsilon = \sqrt{\frac{\alpha_{\max} + \cos \alpha_{\max} \sin \alpha_{\max}}{\alpha_{\max} - \cos \alpha_{\max} \sin \alpha_{\max}}}$$

For a tilt-series with a maximum tilt-angle of $\alpha_{\max} = 65^\circ$ the volume is elongated by a factor $\varepsilon \approx 1.4$ in z-direction. A direct compensation of the measured particle diameter for the elongation factor would result in a value of 1.5 nm for the average particle diameter in z-direction, which is slightly smaller than the diameter measured in the xy-plane. The difference is within the statistical accuracy, but it is probably further enhanced by the fact that the diameter of the small particles is approaching the pixel size of the reconstruction (0.46 nm/pixel). This means that the smallest particles are underestimated, especially in the xy-plane.

Overall, the particle diameter determined from the electron tomography results is slightly larger than the particle size measured by conventional HRTEM measurements in the thinnest sample areas (1.0 to 1.5 nm). This slight difference is due to the resolution of the tomogram, which may be limited by the method itself, but is mostly due to the pixel size of the reconstructed volume. The smallest particle diameters observed by tomography was 1.0 nm, but the number of these small particles is underestimated shifting the measured average particle size to larger values. Nevertheless, the size distribution of particles larger than 1.5 nm will not be affected by the pixel size and reflects the true size variations.

FIGURE 6

These results demonstrate that TEM tomography is a powerful tool to analyze the 3D structure of classical catalysts despite the fact that they are crystalline. As can be seen

in the tilt-series movies, the diffraction contrast in these materials is very low due to the small crystallite size and the high defect density, and, therefore, does not strongly influence the 3D reconstruction. The main advantage of TEM tomography is the short data acquisition time allowing for collection of more data, which becomes crucial in quality control and statistical analysis.

High surface area hydrogen storage medium (HSM)

As shown in Figure 7, the HSM exhibits a complex chemical composition. EDS analysis shows the presence of nickel, magnesium, manganese, cobalt, silicon, and carbon; partially oxidized and partially as a chloride (Figure 7). Even local 2-dimensional EDS mapping with a 1 nm probe does not reveal significant compositional variations within this sample, due to the complex 3D sheet structure.

FIGURE 7

In order to gain a better understanding of the structure and morphology of the HSM, we used TEM tomography. However, as the HSM contains a variety of crystals with a diameter of about 50 nm, the resulting tilt-series show considerable diffraction contrast in some of the 2D projections. Nevertheless, it was possible to align the tilt-series and reconstruct the 3D volume (Figure 8) to show characteristic features of this sample.

FIGURE 8

The 3D reconstruction reveals a structured core in a HSM particle, which consists of domains with different density. Some larger (20 – 70 nm diameter) dense crystals and smaller (10 – 20 nm diameter) low-density areas are visible in the core of the particle, with the lowest density probably representing small pores in the material. In addition, a complex network of high-density platey and fibrous material is visible as well as a large number of small, dense spherical particles (3-4 nm diameter) distributed throughout the core of the HSM particle. This core is surrounded by a low-density layer with fibrils branching off. The extent of this fibrillar structure is unusually large in the example shown in Figure 8, but a layer with some fibrils branching off was observed for all HSM particles analyzed.

Even though a good idea of the overall structure can be developed based on the TEM tomography, this example also shows the limits of TEM tomography for crystalline materials. The 3D reconstruction reveals a clear image of the original object close to the surface of the particle where only limited diffraction contrast is observed in the tilt-series. However, in the center of the particle where several larger crystals are present, the contrast is weak, presumably due to diffraction contrast blurring the features during the back-projection.

In order to reduce the diffraction contribution to the images and thereby obtain a more reliable 3D reconstruction with improved contrast, we used a HAADF-STEM tilt-series as the basis for the 3D reconstruction. At low camera length, no diffraction contrast was observed for the tilt-series, and, furthermore, channeling contrast does not play a major role for this heterogeneous material. The 3D reconstruction based on the HAADF-STEM tomography tilt-series shows the same basic features observed previously by TEM

tomography: a central core consisting of 'large dense' crystals and smaller low-density areas together with a complex network of high-density materials. The small spherical particles are also visible throughout the core. Furthermore, the low-density layer surrounding the core is observed; however, in this case, there are only few fibrils branching off.

FIGURE 9

The contrast in the HAADF-STEM tomogram is significantly better than observed in the previous example due to the combined effects of reduced diffraction contrast as well as the different z-dependence in HAADF-STEM detection. Therefore, identification of the different crystals within the HSM particle is easier and the high-density network can be recognized as interconnecting the large dense crystals and separating domains of low-density. This distribution of the high-density material within the HSM particle is depicted by volume rendering in Figure 10. Furthermore, differences in the low-density material can also be recognized. Two different gray level ranges can be identified for the low-density material, indicating that at least two different low-density materials are present (one of them may represent pores in the material). Even though the detailed interpretation of the density variation in terms of the elemental composition is still subject to further analysis, the tomography results give new insight into the morphology of the HSM particles and unambiguously show that there is enormous available surface area associated with the fibrous and sheet-like microstructures.

FIGURE 10

Semiconductor Devices

In the absence of large single crystalline domains, TEM tomography can be used to characterize the structure of semiconductor devices, e.g. for seed and barrier layer analysis in (unfilled) copper lines (Stegmann and Zschech, 2002). However, in general, the use of BF-TEM tomography is limited for semiconductor devices. Typically, large crystalline grains are present, which give rise to diffraction contrast and bend contours, thereby decreasing the resolution and the contrast in the TEM tomogram. In contrast, HAADF-STEM imaging exhibits only minor diffraction effects, and is, therefore, the preferred general solution for tomography in IC applications. These differences in the resulting reconstruction quality are illustrated using a transistor as an example (Figure 11), which has been reconstructed based on a TEM and a HAADF-STEM tilt-series (Kübel, 2001). The TEM tomography reconstruction shows the general features of the device, but the details are blurred and it is difficult to identify individual defects. However, the contrast in the HAADF-STEM tomography reconstruction is significantly better and individual defects, such as the hole in the cobalt silicide layer and small deposits next to the transistor, can clearly be recognized (Figure 11). For this reason, we used HAADF-STEM tomography for all further semiconductor analysis.

FIGURE 11

Copper Interconnect Lines

Interconnect structures have to be shrunk in advanced logic products to reduce the signal delay on-chip. Current devices have up to 9 layers of horizontal and vertical contact lines stacked on top of the active circuit. The lines have a diameter down to about 200 nm and consist of copper and an ultra-thin barrier layer (e.g. sputtered tantalum) to prevent diffusion of the copper into the active areas of the device. Important aspects of these devices are the diameter and uniformity of the barrier layer, which are difficult to estimate in a single image due to the curvature of the line. Furthermore, small voids during the electrolytic copper filling can be difficult to detect due to their low contrast in the projected image.

FIGURE 12

We have analyzed copper interconnect lines in a modern AMD CPU to evaluate the use of HAADF-STEM tomography to characterize the barrier layer and to detect small voids in the copper. To make sure that some voids were present in the area of interest, we used a sample where the electron beam had generated voids prior to the tomography analysis. The tomogram (Figure 12) shows the barrier layer and the copper of several interconnect lines. The etch-stop layer is also present in the reconstructed volume, but due to the high intensity difference, it cannot be shown together with the tantalum barrier and the copper in an 8-bit gray scale image. Overall, the barrier layer does not change strongly throughout the reconstructed volume, but a detailed analysis shows slight defects in some corners of the interconnect line, where the barrier layer thickness changes or an edge is not completely filled (indicated by circles in Figure 12).

Nevertheless, in no case did copper penetrate the barrier layer during electroplating or the following anneal steps. In addition, several small and some larger voids are visible in the copper (some are indicated by arrows in Figure 12). The larger ones are also visible in the direct 2D projection, but the contrast in an individual projection is not sufficient to observe the smallest voids and tomography is necessary for their detection. The overall structure of the copper interconnect lines with the barrier layer and the etch-stop layer is visualized by surface rendering in Figure 13.

FIGURE 13

Surprisingly, the copper lines show some slight structuring, which seems to coincide with the grain boundaries within the copper lines. We suspect that this is related to diffraction effects at the grain boundaries, which have not been fully suppressed at the camera length used. However, further systematic studies are needed to evaluate how the grain boundaries could be imaged in tomography.

The main limitation of the tomographic reconstruction are artifacts caused by the limited angular sampling and the missing wedge resulting in a faint 'ghost' image of bright and dark lines parallel to the actual interconnect lines. Similar artifacts are presumably present in all tomographic reconstructions, but in the case of HAADF-STEM tomography of sharp, highly regular structures with strong density differences, they become particularly obvious as the intensity of the tantalum barrier layer is roughly a factor of 50 higher than the intensity of the dielectric material in the surrounding background, thereby enhancing any artifacts.

Flash-Memory Cell

Determining and controlling the roughness of interfaces in integrated circuits is becoming increasingly challenging with shrinking device dimensions. In state-of-the-art transistors, gate-oxides have already reached a thickness below 2 nm and their surface roughness needs to be characterized and controlled almost at the atomic level. This is clearly beyond the resolution of current electron tomography techniques, but it is possible to image interfaces with nanometer resolution to detect e.g. spikes resulting in a short circuit. This is illustrated using the analysis of a flash-memory cell by HAADF-STEM tomography as an example.

FIGURE 14

Figure 14 shows a HAADF-STEM image acquired at 0° of a flash-memory cell produced by TSMC. The image shows the overall structure of the memory cell with the floating gate and the control gate as the main components. In the 2D projection, a beacon is visible on the floating gate pointing towards the control gate. This beacon exhibits intensity variations only hinting at a non-uniform structure within the depth of the sample. After 3D reconstruction, the HAADF-STEM tomogram reveals significantly more details about the roughness and shape of the floating and control gates. Four slices in the xy-plane of the reconstructed volume are shown in Figure 15. They reveal the changing shape of the control gate throughout the thickness of the sample. At one position, no beacon is observed, whereas, at a different height, the beacon of the

floating gate is almost in contact with the control gate. The observed structural changes are most pronounced at the beacon of the control gate, but some surface roughness is observed in other areas, especially on top of the control gate. The overall structure of the device and the surface roughness of the control gate is depicted by surface rendering in Figure 16.

FIGURE 15

FIGURE 16

Even though the reconstructed volume shown in Figure 15 reveals significant details about the shape and roughness of the device structure, the weighted back-projection suffers from two problems: First, the 3D reconstruction exhibits considerable noise, which makes automatic identification of the different components difficult. Secondly, the sharp interface with the tungsten via on the left side of the reconstruction leads to similar artifacts as previously observed in the 3D reconstruction of the copper vias, which appear as bright lines in the reconstructed volume. However, as the low-Z material is of interest in this case, the artifacts appear more prominently.

A promising approach to reduce the noise and also the artifacts in the reconstruction are iterative algorithms. Figure 17 shows slices through the volume reconstructed by 20 iterations with SIRT based on the same aligned tilt-series as used for the weighted back-projection in Figure 15. The overall features observed in the volume reconstructed with SIRT are the same as observed in the weighted back-projection. However, the noise is significantly reduced, thereby enabling a much clearer identification of the

materials contrast due to the atomic number (density) differences. The poly-silicon gate structure, the different silicon oxide capping layers and the inter-layer-dielectrics exhibit clear gray scale differences even in the presence of the tungsten via and titanium silicide on top of the control gate (Figure 18). However, it is not possible to differentiate between polysilicon and silicon nitride as both materials exhibited the same scattering strength in the original HAADF-STEM tilt-series images. Interestingly, in most areas, the poly-silicon exhibits a sharp interface with the surrounding oxide. However, some small domains with gray levels intermediate between silicon and silicon oxide are observed, raising the question whether a different chemical composition is present there (circled area in Figure 18). Some artifacts due to the edge of the tungsten via are still present in the SIRT reconstruction and these cause intensity variations in the reconstructed volume. However, in the area indicated in Figure 18, this does not appear to be the reason for the intensity variations observed at the beacon.

Figure 17

Figure 18

Conclusion

Both TEM and HAADF-STEM imaging have some advantages and disadvantages for tomography. For example, TEM image acquisition and the auto-focus are significantly faster (25-40 min.) compared to STEM mode (45-90 min.). On the other hand, by using the dynamic focus option in STEM tomography, it is possible to compensate for the tilt-

induced differences in sample height, which otherwise result in defocus differences across the image in TEM tomography. Therefore, we expect that STEM tomography will ultimately result in a higher resolution than conventional TEM tomography. Another consideration is the different Z-dependence, which scales approximately with $Z^{3/4}$ for TEM compared to $Z^{1.7-2}$ for HAADF-STEM imaging. Thus, if the structure of low-Z materials is to be imaged in the presence of high-Z materials, TEM tomography will make better use of the dynamic range of the images, whereas HAADF-STEM tomography is best suited to visualize high-Z materials (in a light matrix). As an example, the location of 0.8 nm nano gold markers on hair cell stereocilia could be visualized after reconstruction of a HAADF-STEM tomography series, whereas the nano gold was not visible in a TEM tomography reconstruction of the same area (Ziese et al. 2002).

Despite these arguments, the most crucial difference between TEM and HAADF-STEM tomography is the ability to work with highly crystalline materials by using HAADF-STEM imaging. The examples in this paper show that some diffraction contrast can be tolerated in TEM tomography, meaning that most catalysts can be imaged by TEM tomography. However, as the crystallite size within the sample increases, TEM tomography becomes more limited. Crystals with a diameter of about 50 nm already induce noticeable blurring in the 3D reconstruction of the HSM and larger crystalline domains, as encountered in the transistor, prevent any reliable 3D reconstruction. In contrast, HAADF-STEM tomography was not noticeably limited by diffraction contrast or channeling effects, even in case of highly crystalline samples such as the copper lines or the flash memory cell.

Some artifacts are present in the 3D reconstructions due to the limited angular sampling and the missing wedge during data acquisition. These artifacts are particularly visible in 3D reconstructions of semiconductor devices due to their strong density differences and sharp interfaces in the devices. However, the iterative reconstruction algorithm SIRT reduces these artifacts and significantly reduces the noise in the reconstructed volume, which is an important step towards the automatic identification of materials within the reconstructed volume.

Both by using TEM and HAADF-STEM tomography in materials science, features with dimensions on the order of 2 to 3 nm can be observed on a routine basis even for relatively thick samples of 150 to 400 nm. In addition, even below the 2 nm level, it is possible to measure size distributions accurately down to a diameter of at least 1.5 nm and detect particles with a diameter of 1 nm. With this resolution, electron tomography has the potential to help provide answers to a wide range of characterization challenges in the physical sciences.

Acknowledgements

The authors would like to thank Anne-Mette Heie Kjær for sample preparation of the catalyst #1 and Dr. Jennifer Dean for editing the manuscript. Dr. John Bradley's work was performed under the auspices of the U.S. Department of Energy, National Nuclear Security Administration by the University of California, Lawrence Livermore National Laboratory under contract No. W-7405-Eng-48.

References

- Batson, P.E. (1999). Advanced spatially resolved EELS in the STEM. *Ultramicroscopy* **78**, 33-42.
- Baumeister, W., Grimm, R., Walz, J. (1999). Electron tomography of molecules and cells. *Trends Cell Biol.* **9**, 81-85.
- Breyse, M., Afanasiev, P., Geantet, P., Vrinat, M. (2003). Overview of support effects in hydrotreating catalysts. *Catalysis Today*, **86**, 5-16
- Browning, N.D., Pennycook, S.J. (2000). *Characterization of High T_C Materials and Devices by Electron Microscopy*. Cambridge, UK: Cambridge University Press.
- Buseck, P.R., Dunin-Borkowski, R.E., Devouard, B., Frankel, R.B., McCartney, M.R., Midgley, P.A., Pósfai, M., Weyland, M. (2001), Magnetite Morphology and Life on Mars. *Proc. Nat. Acad. Sci.* **99**, 13490-13495.
- Dhar, G.M., Srinivas, B. N., Rana, M. S., Kumar, M. Maity, S. K., (2003). Mixed oxide supported hydrodesulfurization catalysts—a review. *Catalysis Today*, **86**, 45-60.
- Fetcenko, M.A., Ovshinsky, S.R., Reichman, B., Young, K., Chao, B., Im, J., (1997) *United States Patent* 5,616,432.
- Fetcenko, M.A., Ovshinsky, S.R., Reichman, B., Young, K., Chao, B., Im, J., (2003) *United States Patent Pending* 10/733,702.
- Frank, J. (1992). *Electron Tomography: Three-dimensional imaging with the transmission electron microscope*. New York, USA: Plenum Press.
- Gilbert P. (1972) Iterative Methods for the Three-dimensional Reconstruction of an Object from Projections. *J. Theo. Biol.* **36**, 105-117.

- Gilbert, P.F.C. (1972). The reconstruction of a three-dimensional structure from projections and its application to electron microscopy. II Direct methods. *Proc. R. Soc. London* **B182**, 89-102.
- James, E.M., Browning, N.D. (1999). Practical aspects of atomic resolution imaging and analysis in STEM. *Ultramicroscopy* **78**, 125-139.
- Jia, C.L., Lentzen, M., Urban, K. (2003). Atomic-Resolution Imaging of Oxygen in Perovskite Ceramics. *Science* **299**, 870-873.
- Kisielowski, C., Hetherington, C.J.D., Wang, Y.C., Kilaas, R., O'Keefe, M.A., Thust, A. (2001). Imaging columns of the light elements carbon, nitrogen and oxygen with sub Ångstrom resolution. *Ultramicroscopy* **80**, 243-263.
- Koster, A.J., van den Bos, A., van der Mast, K.D. (1987). An autofocus method for a TEM. *Ultramicroscopy* **21**, 209-221.
- Koster, A.J., Klumperman, J. (2003). Electron microscopy in cell biology: integrating structure und function. *Supplement Nature Reviews Cell Biology* **2003:4**, SS6-SS10.
- Koster, A.J., Ziese, U., Verkleij, A.J., Janssen, De Jong, K.P. (2000). Three-dimensional electron microscopy: a novel imaging and characterization technique with nanometer scale resolution for materials science. *J. Phys. Chem. B* **104**, 9368-9370.
- Kübel, C. (2001) Application of electron tomography for materials science. Tomography Workshop of the Koninklijke Nederlandse Akademie van Wetenschappen, Amsterdam.
- Lee, T.-C., Huang, J.-Y., Chen, L.-C., Hwang, R.-L., Su, D. (2002). Methodology for TEM analysis of barrier profiles. ISTFA conference, 2002.

- McEwen, B.F. Marko, M. (2001). The Emergence of Electron Tomography as an Important Tool for Investigating Cellular Ultrastructure. *J. Histochem. Cytochem.* **49(5)**, 553-563.
- McIntosh, J.R. (2001); Electron Microscopy of Cells: A New Beginning for a New Century. *J. Cell Biol.* **153**, F25-F32.
- Midgley, P.A., Weyland, M. (2003). 3D electron microscopy in the physical sciences: the development of Z-contrast and EFTEM tomography. *Ultramicroscopy* **96**, 413-431.
- Muller, D.A., Sorsch, T. , Moccio, S., Baumann, F. H., Evans-Lutterodt, K., Timp, G. (1999). The electronic structure at the atomic scale of ultrathin gate oxides. *Nature*, 399, 758-761.
- Rademacher, M. (1988). 3-dimensional reconstruction of single particles from random and nonrandom tilt-series. *J Electron Microsc. Tech.* **9**, 359-394.
- Sali, A.; Glaeser, R., Earnest, T., Baumeister, W. (2003). From words to literature in structural proteomics. *Nature* **422**, 216-225.
- Spence, J. (2002). Achieving atomic resolution. *MaterialsToday* **2002:3**, 20-33.
- Stegmann, H., Zschech, E. (2002). Electron tomography of semiconductor copper interconnect structures. *G.I.T. Imaging & Microscopy* 4/2002, 8-9.
- Voyles, P.M., Muller, D. A., Grazul, J. L., Citrin, P. H., Gossmann, H.-J. L. (2002) Atomic-scale Imaging of Individual Dopant Atoms and Clusters in Highly *n*-type Si. *Nature* **416**, 826.
- Weyland, M. (2001) *Two and Three Dimensional Nanoscale Analysis: New Techniques and Applications*. Ph.D. Thesis, Cambridge, UK.

- Weyland, M., Midgley, P.A., Thomas, J.M. (2001). Electron Tomography of Nanoparticle Catalysts on Porous Supports: A New Technique Based on Rutherford Scattering. *J. Phys. Chem.* **B105**, 7882-7886.
- Weyland, M., Midgley, P.A. (2003) Extending Energy-Filtered Transmission Electron Microscopy (EFTEM) into Three Dimensions Using Electron Tomography. *Microsc, Microanal.* **9**, 542-555.
- Young, R.J., Carleson, P.D., Da, X., Hunt, T., Walker, J.F. (1998). High-Yield High-Throughput TEM Sample Preparation Using Focus Ion Beam Automation. *Proceedings from the 24th International Symposium for Testing and Failure Analysis, 15-19 November, Dallas, Texas.*
- Ziese, U., Kübel, C., Verkleij, A.J., Koster, A.J. (2002) Three-dimensional localization of ultra-small immuno-gold labels by HAADF-STEM Tomography. *J. Struct. Biol.* **138**, 58-62.
- Ziese, U., Janssen, A.H., Murk, J.L., Geerts, W.J., Van der Krift, T., Verkleij, A.J., Koster, A.J. (2002). Automated high-throughput electron tomography by pre-calibration of image shifts. *J. Microsc.* **205**, 187-200.
- Zschech, E., Engelmann, H.-J., Stegmann, H., Saage, H., de Robillard, Q. (2003). Barrier/seed step coverage analysis in via structures for inlaid copper process control. *Future Fab Intl.* **14**.

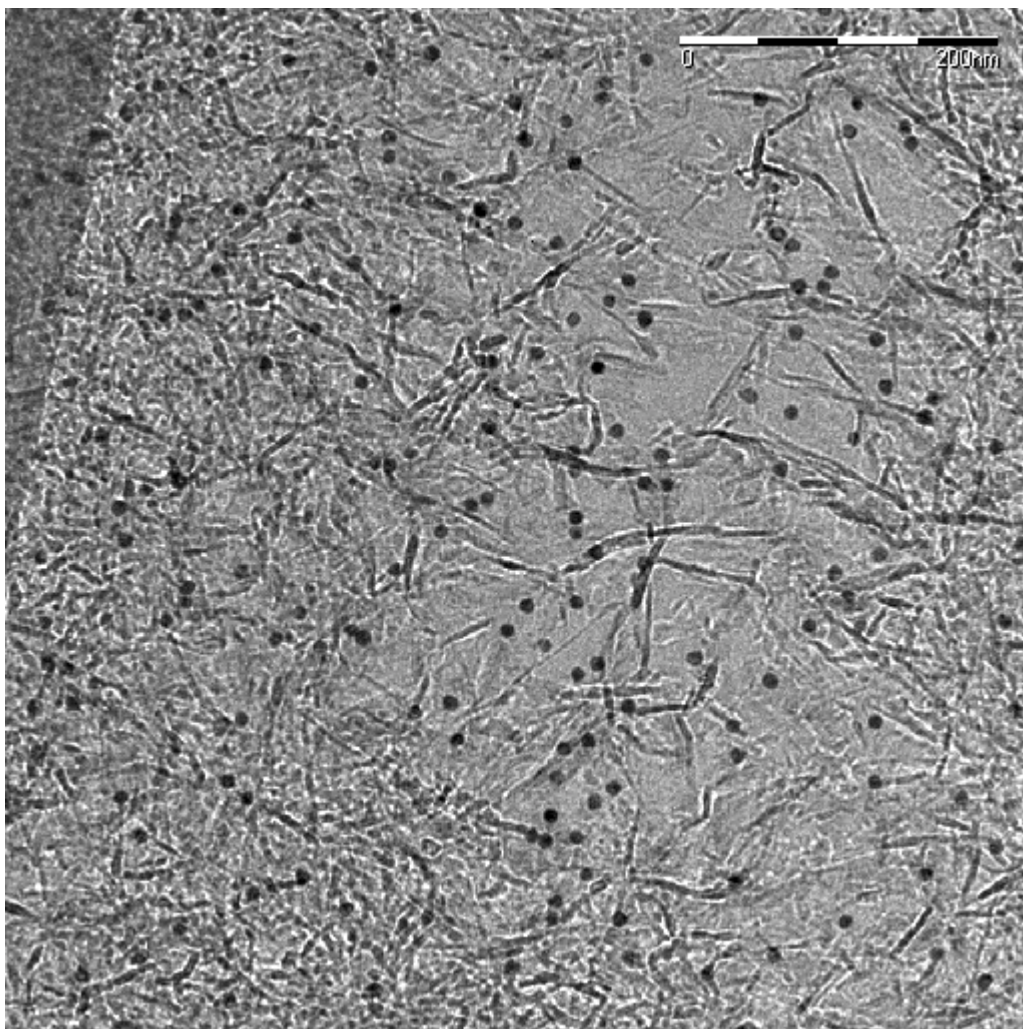


Figure 1: TEM image of a catalyst produced by Topsoe for oil refining. The projected image reveals a lower density of the support material (large pore) in the center. The larger dark particles are 10 nm gold markers used for tomography alignment later.

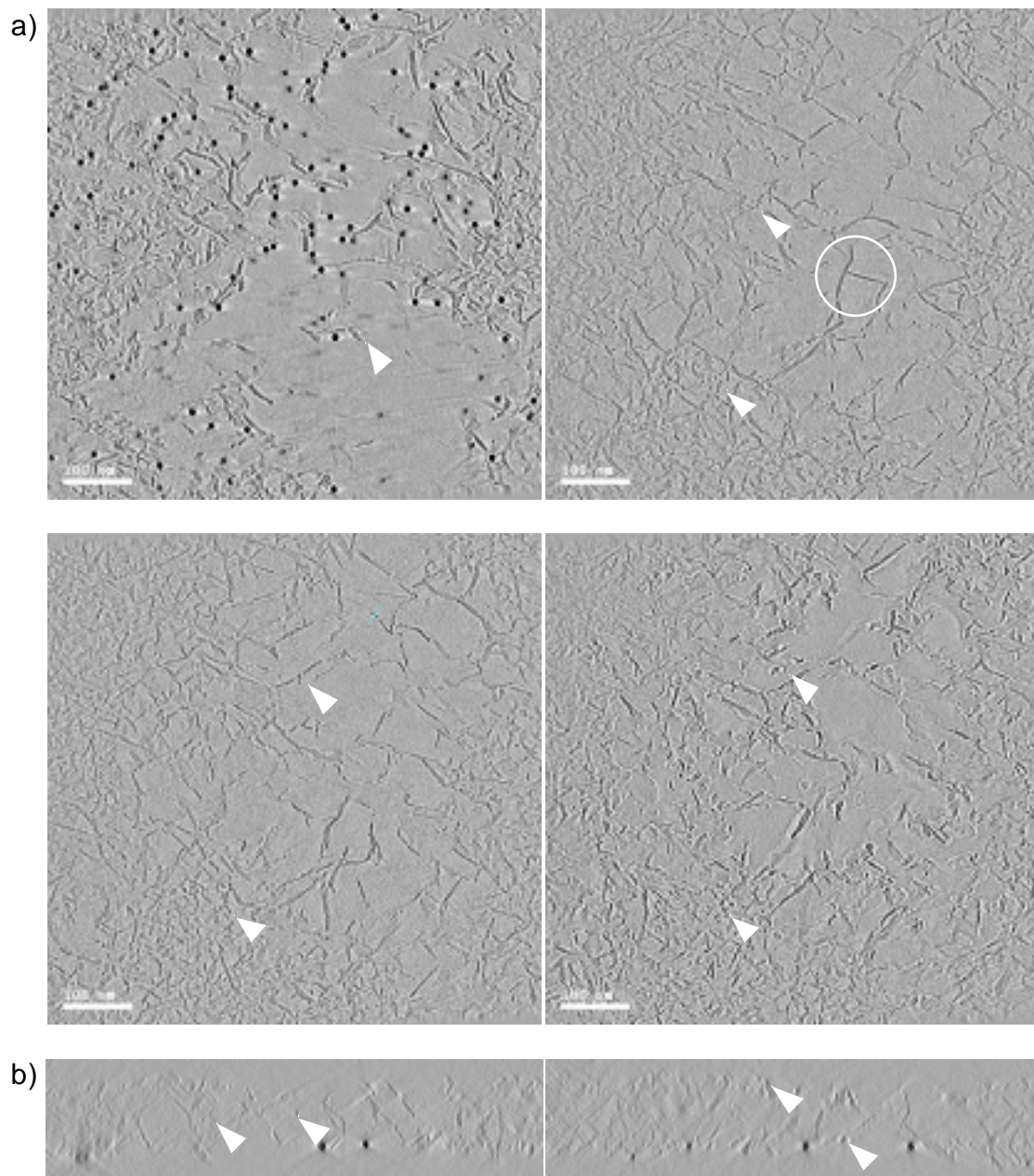


Figure 2: a) XY slices spaced approximately 20 nm in z through the 3-D reconstructed volume of the catalyst shown in Figure 1. In the large central pore, large sheets of the support material are predominately visible, whereas small sheets of the support material are mainly present in the dense areas. The catalyst particles themselves are also visible as small dark “spots” on the

support material. The arrows indicate a few of the many catalyst particles and the circle shows the area used for surface rendering of a support sheet in Figure 3.

b) XZ slices from the center and the edge of the 3-D reconstructed volume of the catalyst.

(A movie showing all x-y slices through the reconstructed volume is available as support material).

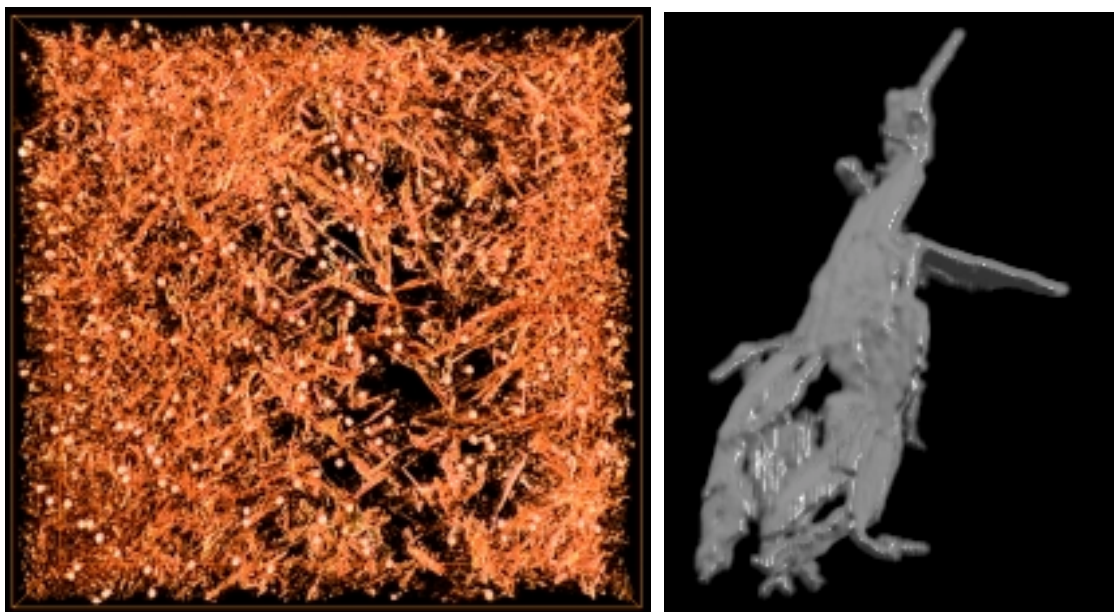


Figure 3: Volume rendering of the overall structure of the support material and surface rendering (area indicated by a white circle in Figure 2) showing details of the sheet-like structure of the support material.
(A movie showing the surface rendering of the alumina support sheet is available as supporting material).

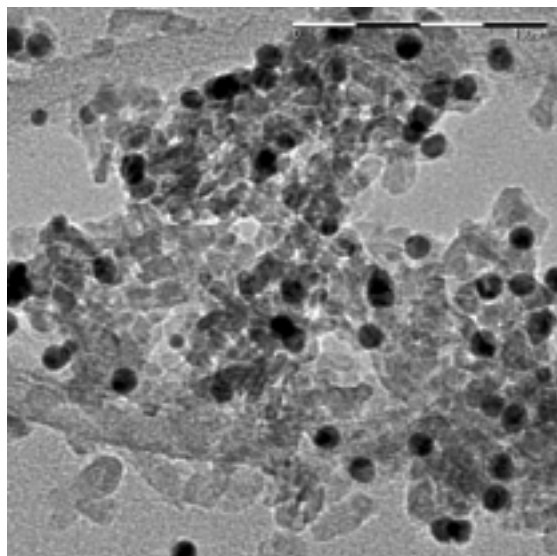


Figure 4: TEM projection of an alumina based catalyst with Pt nano-particles recorded at 10° tilt. The projection reveals the support material and the gold markers used for image alignment. The active Pt-catalyst particles are also visible, but it is difficult to identify them unambiguously in the projection. (A movie showing the aligned tilt-series is available as supporting material).

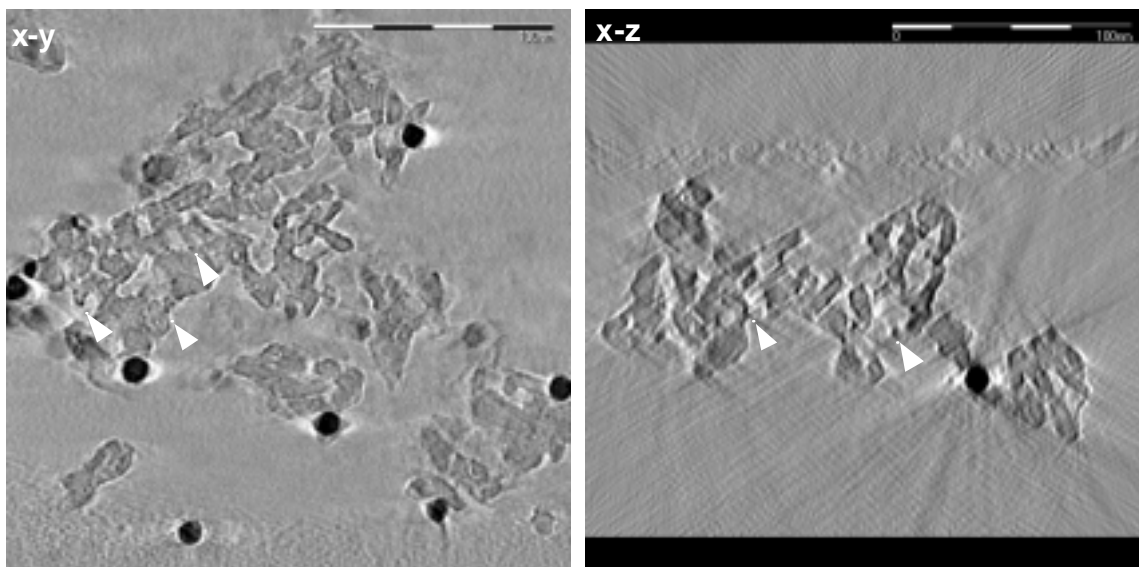
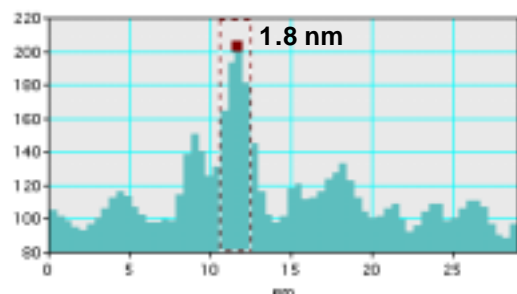
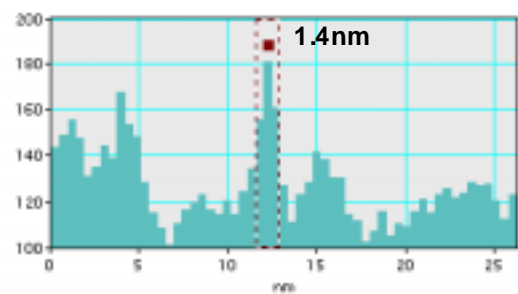
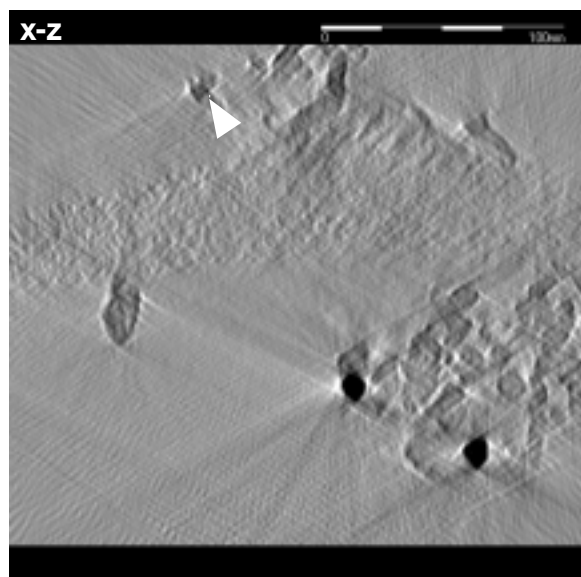
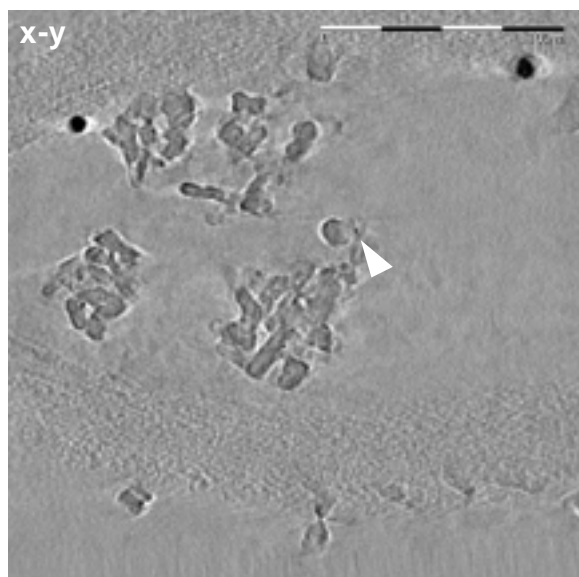


Figure 5: x-y and x-z slices through the reconstructed volume of the catalyst shown in Figure 4. The reconstruction shows the network formed by the alumina support and a large number of Pt catalyst particles (some of them indicated by arrows) as well as several large gold labels. The Pt catalyst particles can be clearly identified in the reconstructed volume due to the improved contrast in the 3-D reconstruction compared to each individual 2D projection. (Movies showing all x-y and x-z slices through the reconstructed volume are available as support material).

a)



b)

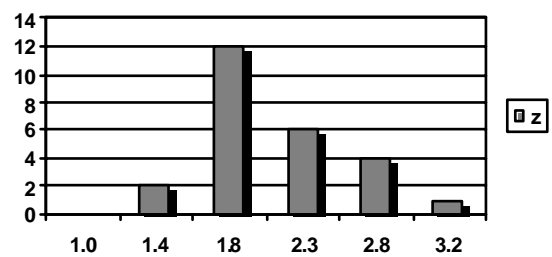
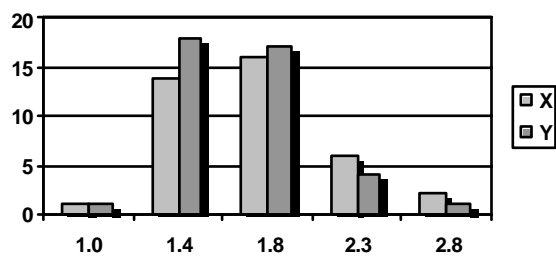
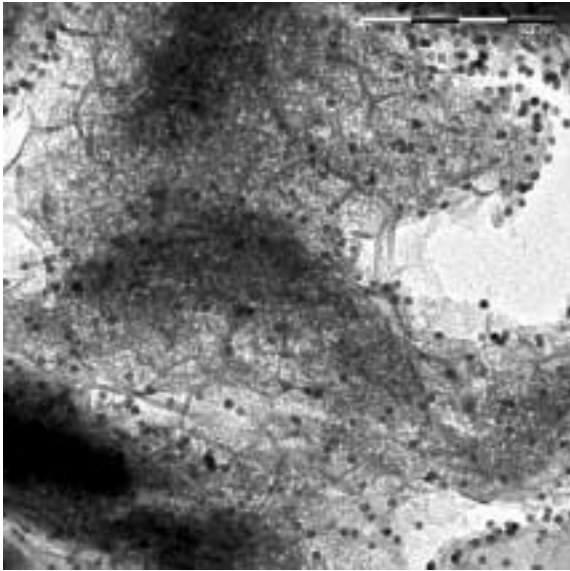


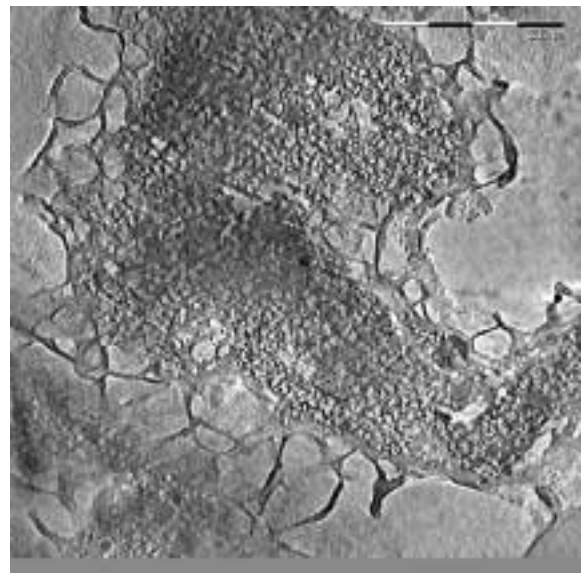
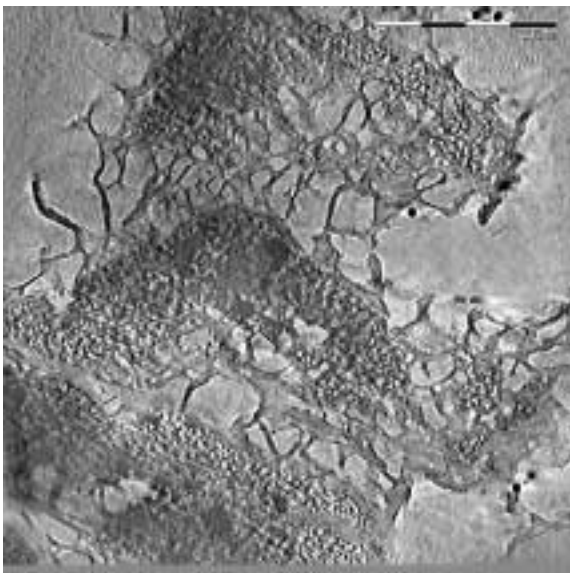
Figure 6: a) x-y and x-z slices through the reconstructed volume of the catalyst shown in Figure 4. The diameter of 25-40 Pt particles was analyzed by line profiles along the main directions for a statistical analysis. The FWHM of the line profile was used to estimate the particle diameter; the values for the particle diameter in z-direction are not corrected for any elongation due to the missing wedge.

b) Particle diameter distribution measured along the main directions from several slices through the reconstructed volume (Figure 5 and 6a).

a)



b)



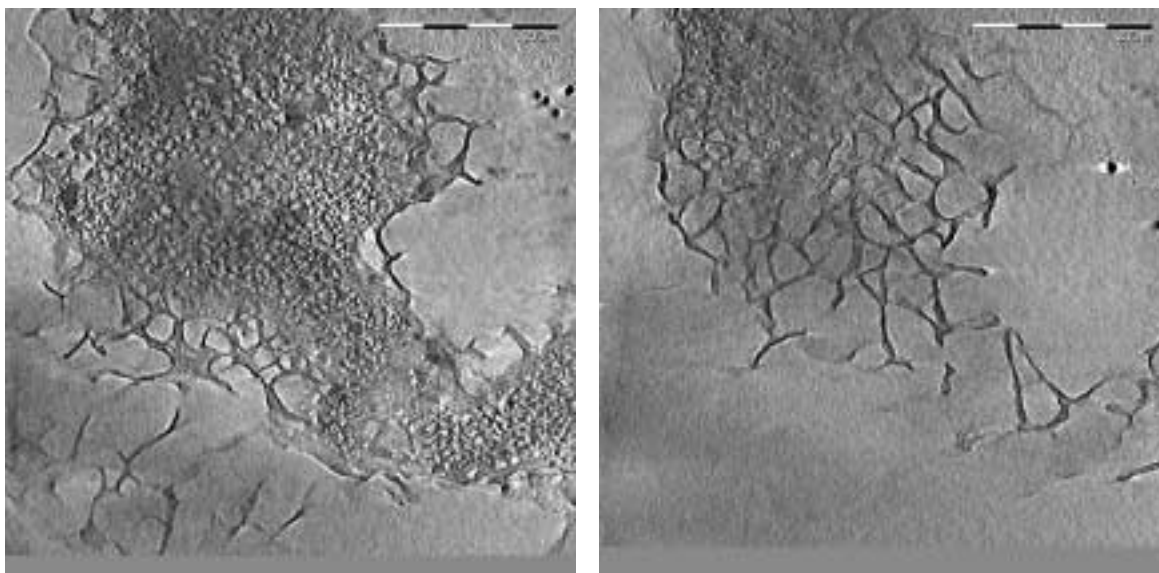
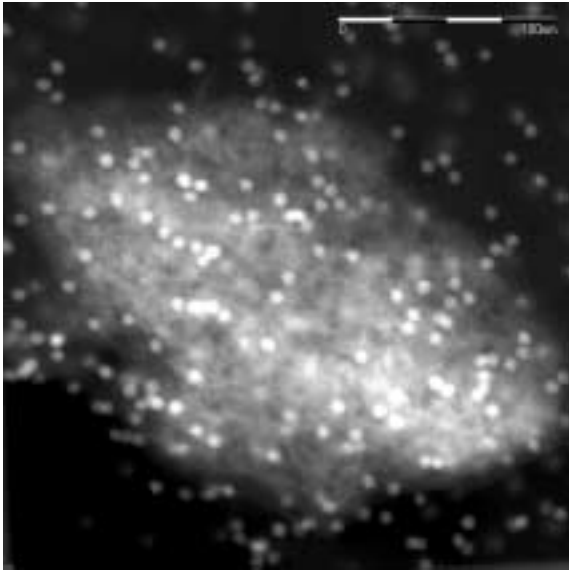


Figure 8: a) TEM projection of a HSM particle at 0° tilt angle. The round particles visible everywhere in the projection are the gold markers applied for the tilt-series alignment.

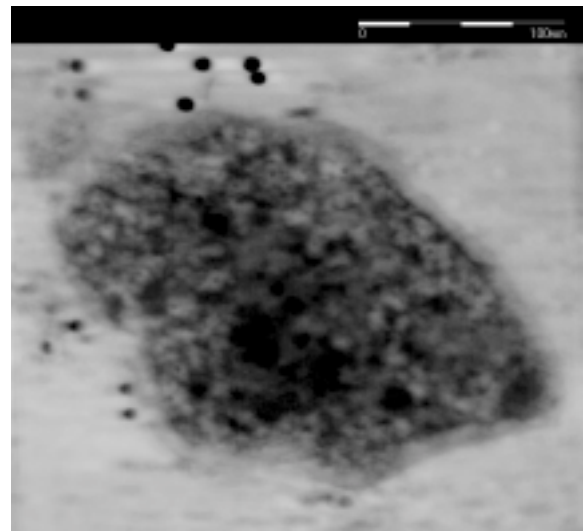
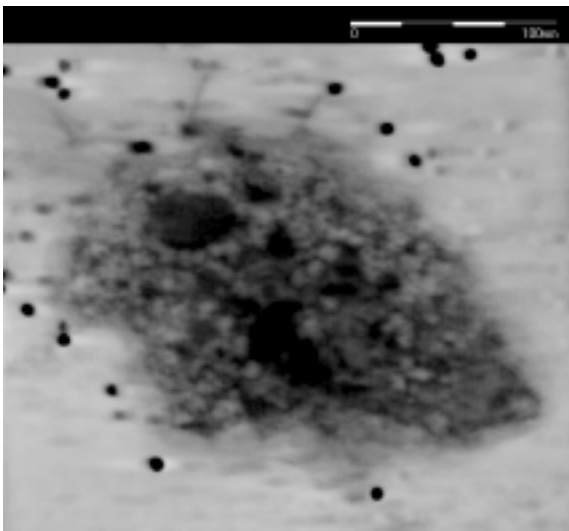
b) 4 slices in the xy plane of the reconstructed volume of the HSM particle. The core of the particle is highly structured consisting of domains with different density. Some larger dense crystals and a lot of small low-density areas are visible together with a complex network of high-density material. In addition, a large number of very small (3-4 nm diameter) spherical particles are distributed throughout the HSM particle. This core of the particle is surrounded by a low-density layer with a lot of fibrils branching off.

(A movie showing the aligned tilt-series and slices through the reconstructed volume is available as supporting material).

a)



b)



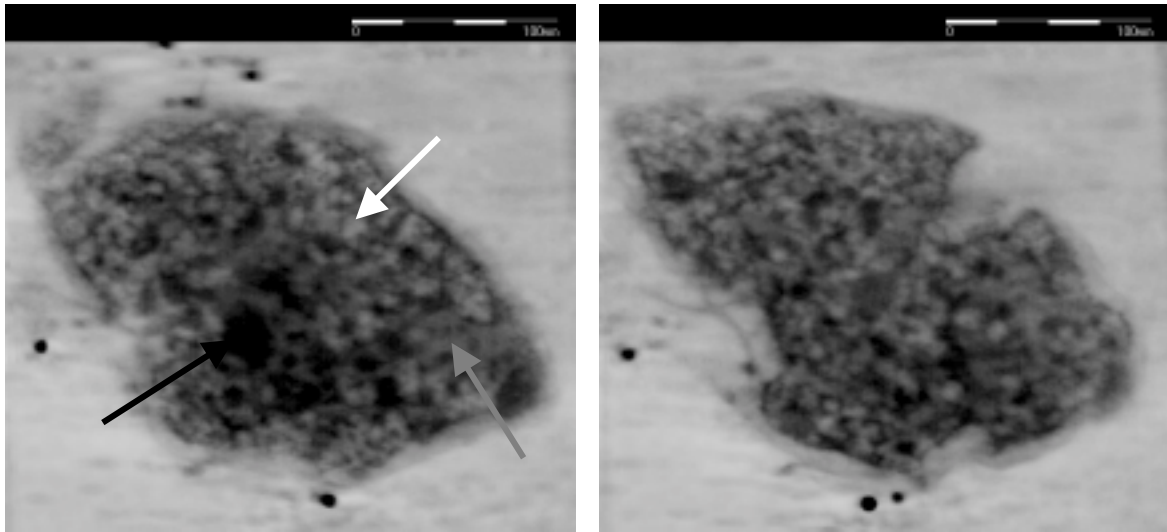


Figure 9: a) HAADF-STEM projection of a HSM particle at 0° tilt angle. The bright particles visible everywhere in the projection are the 10 nm gold markers applied for the tilt-series alignment.

b) 4 slices in the xy plane of the reconstructed volume of the HSM particle (contrast inverted compared to the original HAADF-STEM images). The HSM particle is highly structured consisting of domains with different density. Three different gray level ranges can be distinguished in the reconstruction (exemplified by arrows in one of the slices) indicating the presence of at least three different materials. Large dense crystals with a diameter of 10 – 50 nm as well as dense, spherical particles with a diameter of 2 – 4 nm are visible. Two different lower-density domains can be distinguished; a complex network of high-density material typically forms the boundary between adjacent domains. This core of the particle is surrounded by a low-density layer with a few fibrils branching off.

(A movie showing the aligned tilt-series and slices through the reconstructed volume is available as supporting material).

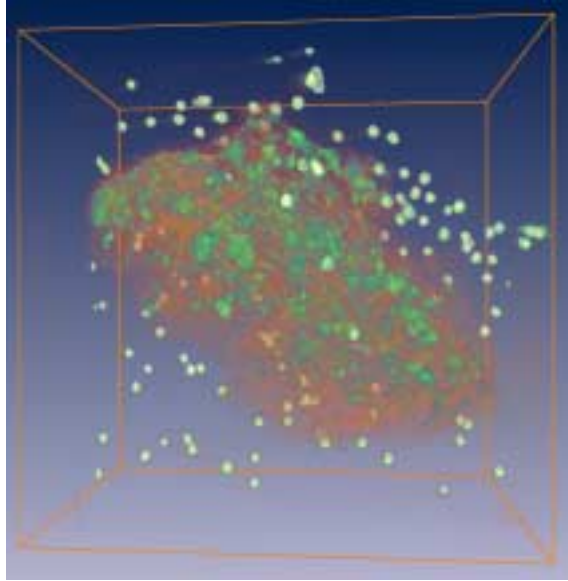
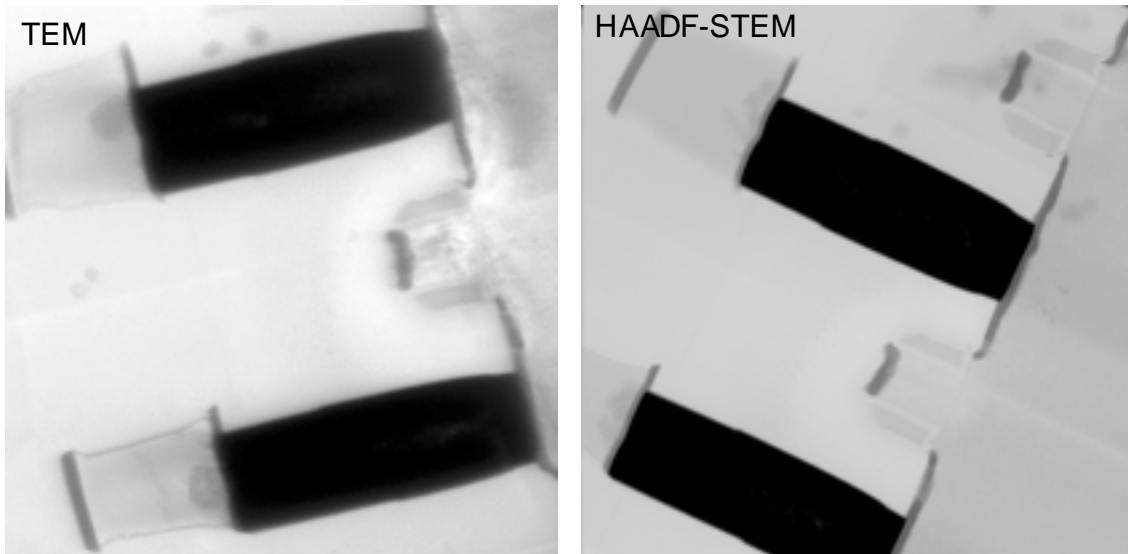


Figure 10: Volume rendering based on the HAADF-STEM tomogram in showing the 3D distribution of the high-density domains (green) within a HSM particle (orange) together with the gold particles (greenish white). (A movie showing the 3D rendering from different angles is available as supporting material).

a)



b)

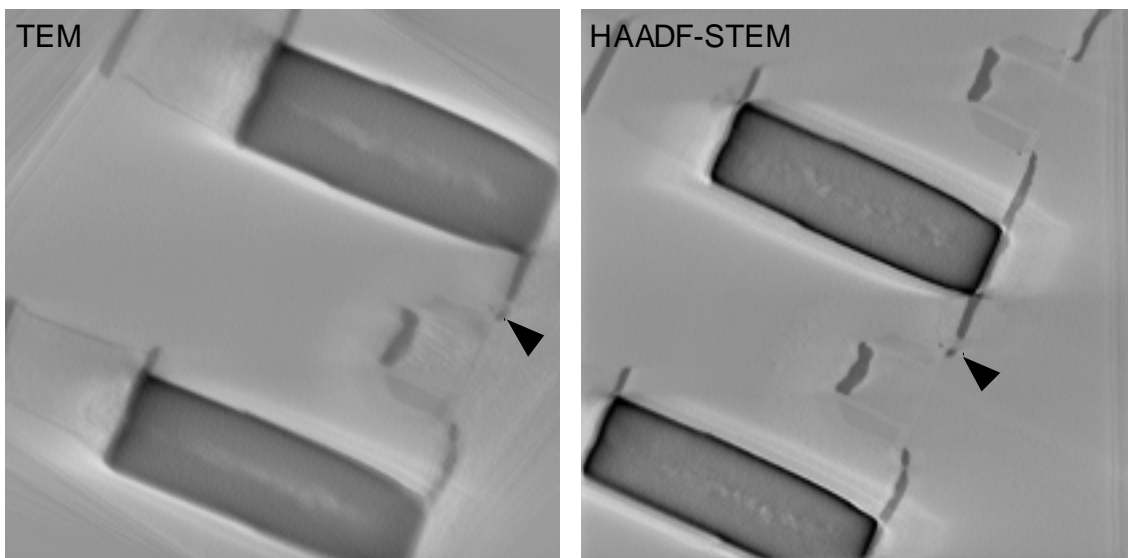
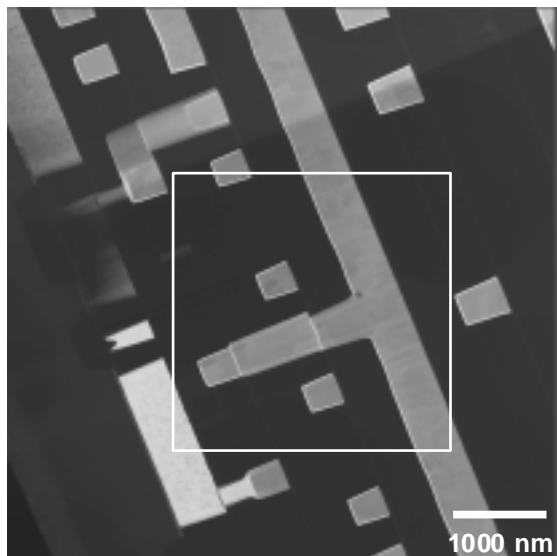


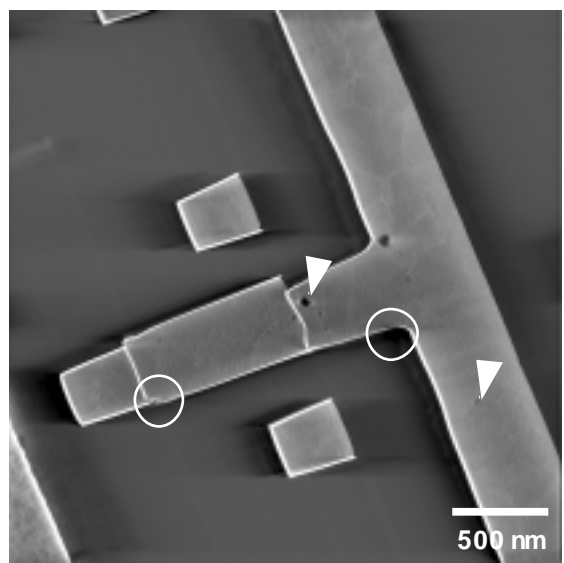
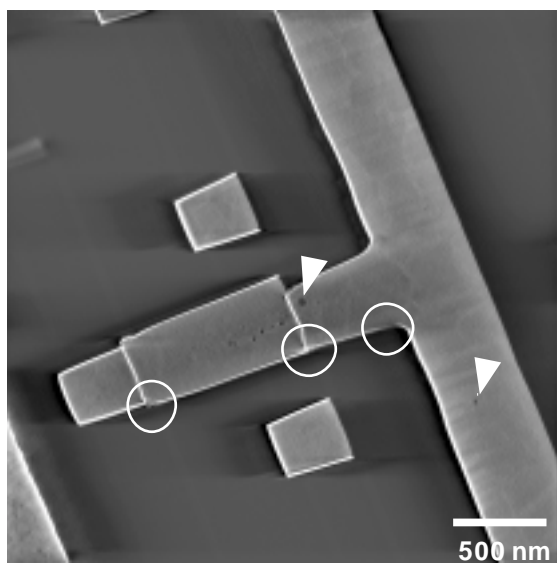
Figure 11: a) TEM and (inverted) HAADF-STEM image of a transistor and tungsten connects. The TEM image exhibits strong diffraction contrast and bend contours, which are greatly reduced by HAADF-STEM imaging.
b) 3D reconstruction based on the TEM and (inverted) HAADF-STEM tilt-series. The images show a slice in the xy-plane through the reconstructed

volume at the same position in the sample. The acquisition geometry and the alignment quality were identical in both cases, but the HAADF-STEM results show significantly more and much clearer details compared to the TEM tomography data. The HAADF-STEM tomogram reveals e.g. a hole in the cobaltsilicide layer (indicated by the black arrow) and several small deposits next to the transistor. (Kübel, 2001)

a)



b)



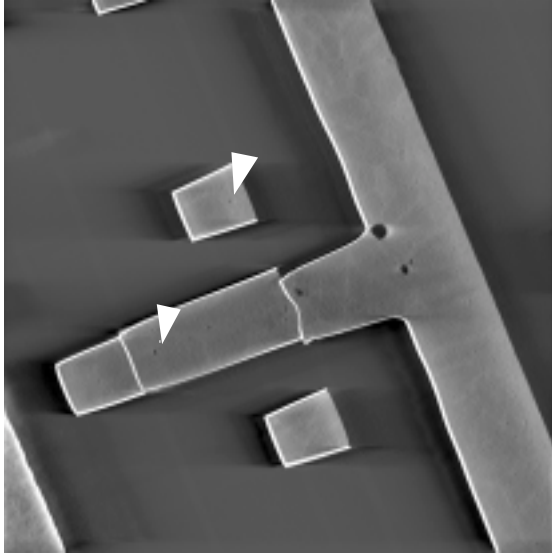


Figure 12: a) HAADF-STEM image acquired at 0° tilt, showing copper lines in a modern AMD CPU.

b) 3D tomographic reconstruction of copper lines based on the HAADF-STEM tilt-series. The xy slices through the reconstructed volume show the tantalum barrier layer and the copper filling of the lines. The arrows indicate some of the small voids generated in the copper lines. The circles indicate some defects in the barrier layer; nevertheless no copper penetrated the barrier layer.

(A movie showing the aligned tilt-series and a movie of the reconstructed volume are available as supporting material).

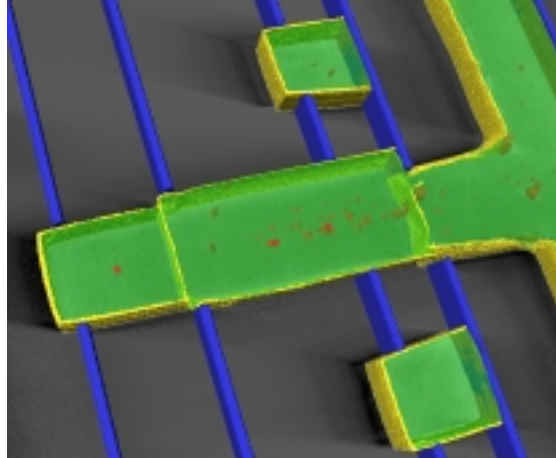


Figure 13: Surface rendering based on the HAADF-STEM tomogram showing the 3D structure of the interconnect lines with some bending and slight variations of the tantalum barrier layer (yellow). The copper is depicted green and the 3D distribution of the voids within the copper is shown in red. The etch-stop layer is depicted blue.

(A movie showing the 3D rendering from different angles is available as supporting material).

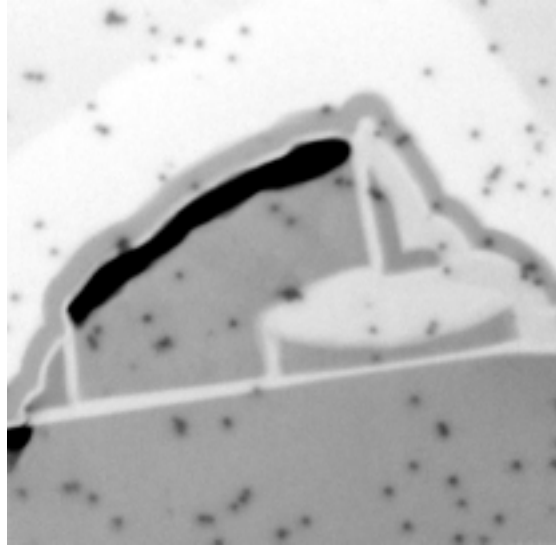


Figure 14: HAADF-STEM image of a flash memory cell produced by TSMC (contrast inverted). The image shows the floating and the reference gate of the memory cell as the main components of the storage device. Furthermore, a large number of gold markers are visible, which were used for alignment of the tilt-series.

(A movie showing the aligned tilt-series and a movie of the reconstructed volume are available as supporting material).

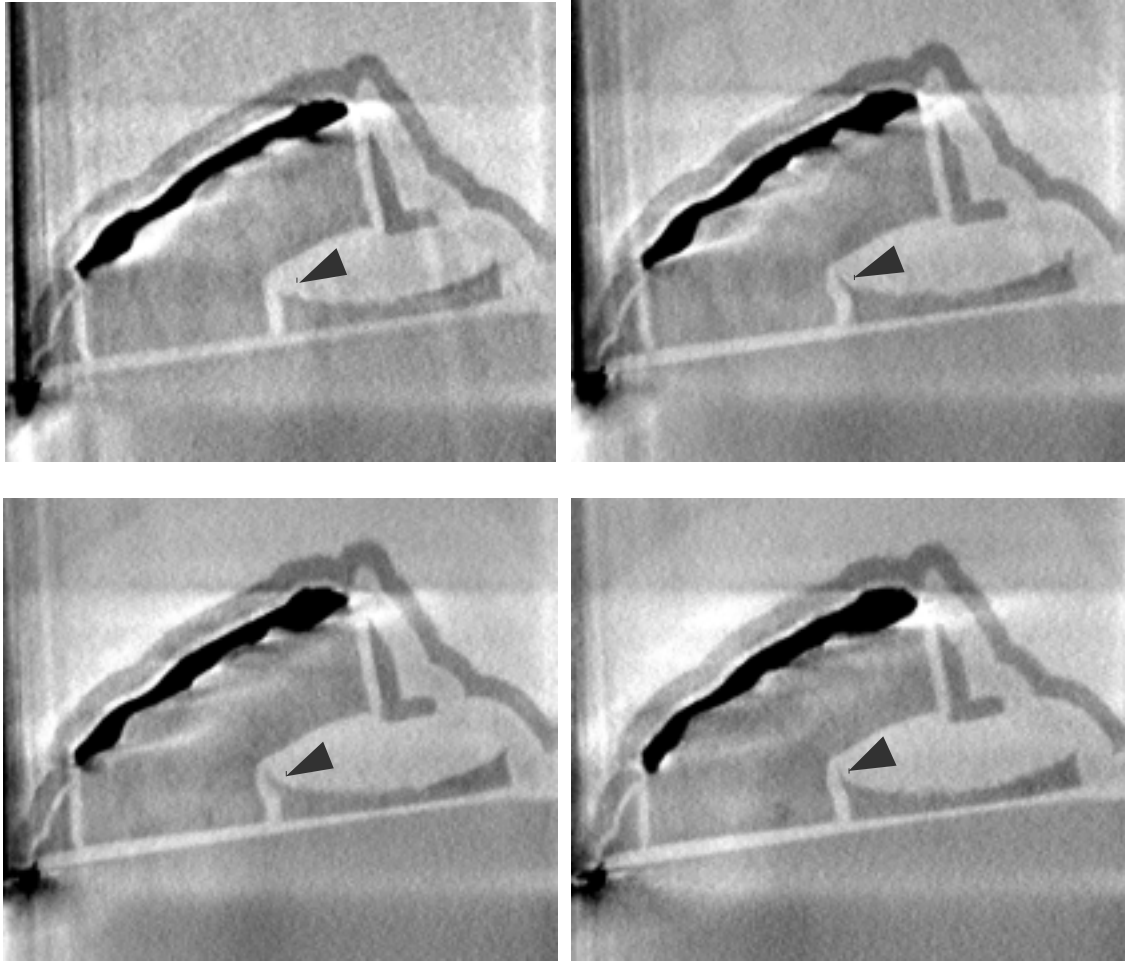


Figure 15: 3D tomographic reconstruction of a flash memory cell based on an (inverted) HAADF-STEM tilt-series. The xy slices through the reconstructed volume show the poly-silicon floating gate and the reference gate on top of the silicon wafer as the main components of the storage device. In addition, the edge of the tungsten via is visible on the left side. The 3D reconstruction reveals the changing shape of the floating gate, especially the shape of the beacon pointing towards the reference gate (indicated by a black arrow). Furthermore, the surface roughness on the topside of the floating gate is visible in these slices.

(A movie showing the aligned tilt-series and a movie of the reconstructed volume are available as supporting material).

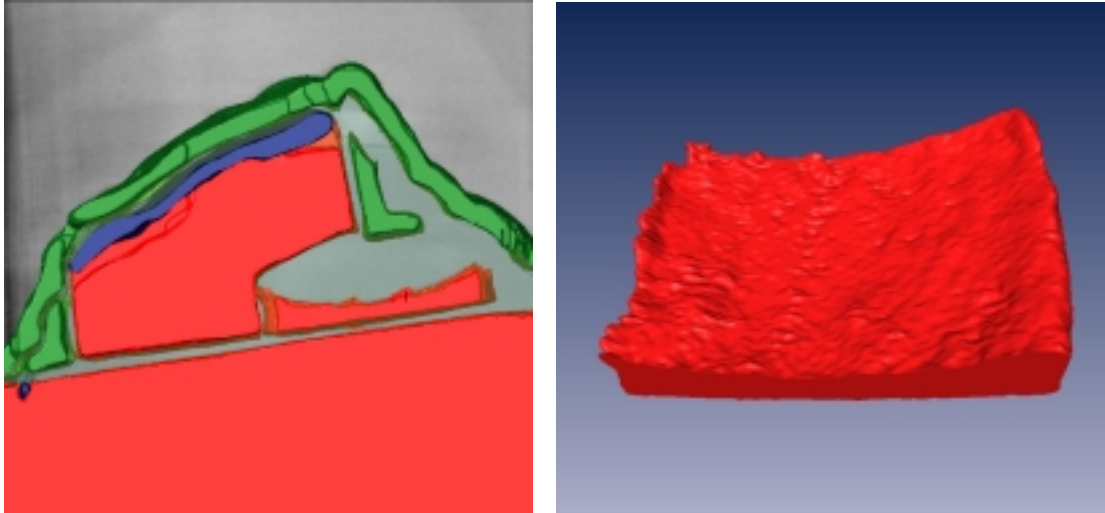


Figure 16: a) Surface rendering showing the overall 3D structure of the memory cell based on the volume obtained by weighted back-projection (silicon: red, silicon nitride: green, titanium silicide: blue).
b) Surface rendering of the floating gate showing the roughness at the top of the gate based on the SIRT reconstruction.

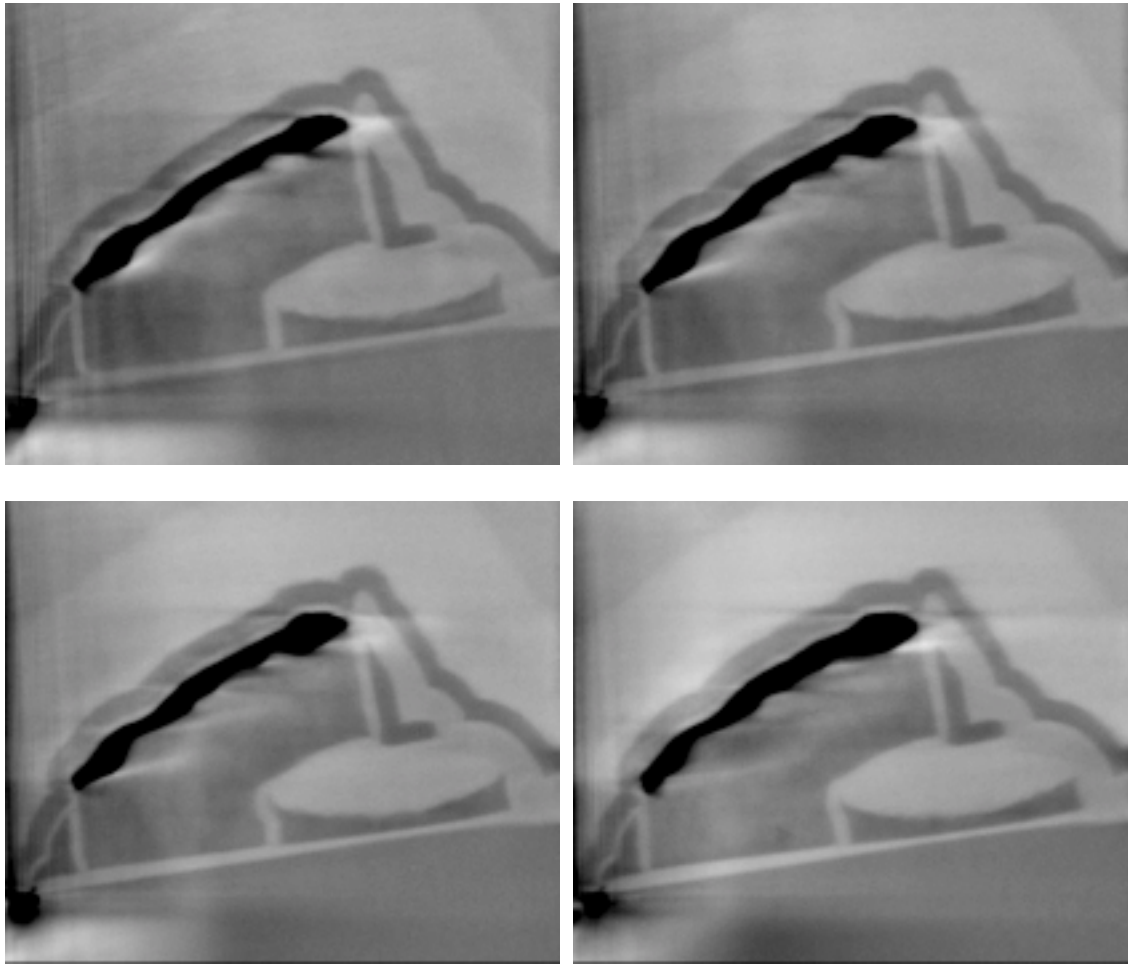


Figure 17: 3D tomographic reconstruction using a SIRT algorithm with the same aligned tilt-series as used in Figure 15. Slices in the xy-plane of the reconstructed are shown approximately at the same position as in Figure 15. In principle, the volume reconstructed with SIRT shows the same features as the volume obtained by weighted back-projection. However, the noise in the reconstruction is significantly lower enabling a clearer detection of the atomic number contrast between the different parts of the device. (A movie showing the aligned tilt-series and a movie of the reconstructed volume are available as supporting material).

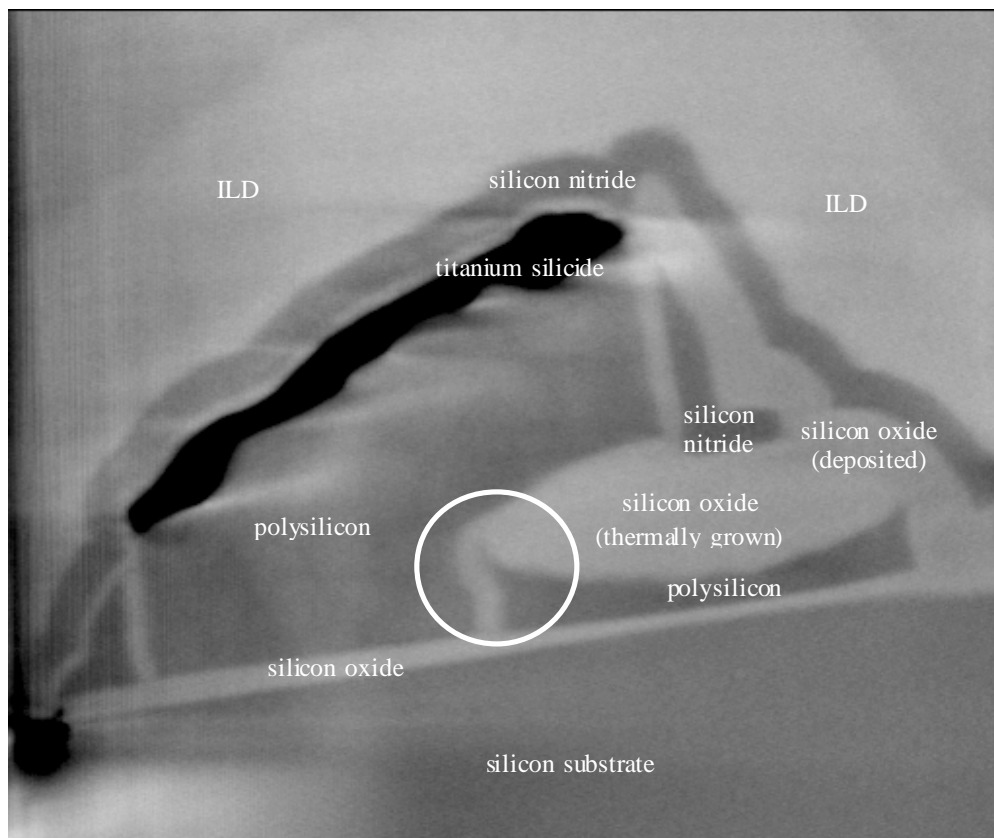


Figure 18: The volume reconstructed by SIRT reveals clear graylevel differences due to differences in density and chemical composition, thus enabling observation of the thermally grown and deposited silicon oxide as well as the inter-layer-dielectric (ILD). The small scattering strength differences of the silicon oxides can be visualized even though the dynamic range of the HAADF-STEM detector was optimized to cover the full intensity range of the heavy elements titanium silicide and tungsten. However, it is not possible to differentiate between polysilicon and silicon nitride as both materials also appear the same in the original HAADF-STEM images.